Journal Pre-proof

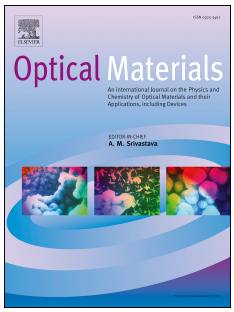

Ray scattering in fiber-reinforced transparent wood composites – wood microstructural effects and virtual camera simulations

Bin Chen, Sergei Popov, Lars A. Berglund

PII: S0925-3467(25)00313-1

DOI: https://doi.org/10.1016/j.optmat.2025.116953

Reference: OPTMAT 116953

To appear in: *Optical Materials*

Received Date: 20 January 2025

Revised Date: 15 March 2025

Accepted Date: 16 March 2025

Please cite this article as: B. Chen, S. Popov, L.A. Berglund, Ray scattering in fiber-reinforced transparent wood composites – wood microstructural effects and virtual camera simulations, *Optical Materials*, https://doi.org/10.1016/j.optmat.2025.116953.

Ray scattering in fiber-reinforced transparent wood composites – wood microstructural effects and virtual camera simulations

Bin Chen[1,*], Sergei Popov[2], Lars A. Berglund[1]
Email: binchen@kth.se

1. Wallenberg Wood Science Center, Department of Fibre and Polymer Technology, KTH Royal Institute of Technology, SE-10044 Stockholm, Sweden
2. SCI school, Applied Physics Department, KTH Royal Institute of Technology, SE-11419 Stockholm, Sweden

Abstract: Transparent wood (TW) is a sustainable composite material with high optical transmittance and excellent mechanical properties. Nanoparticles, dyes and quantum dots can be added in a controlled manner for new functionalities relying on the light scattering properties of the composite. The scattering properties of 3D TW models of cellular microstructure are investigated numerically using geometrical optics. A group of 3D TW material models with controlled microstructural parameters are generated based on an analytical method. A ray tracing approach is adopted to model scattering in these complex materials. Effects from different material parameters on ray scattering are analyzed. A virtual camera or virtual eye to render images positioned behind a TW plate is simulated using backward ray tracing. The blurred impression in human eyes of real objects viewed through a TW "window" can then be mimicked.

Keywords: transparent wood; ray scattering; backward ray tracing; virtual camera

1. Introduction

Transparent wood (TW) is a sustainable multifunctional composite that combines high optical transparency and excellent mechanical properties [1]. Usually, such materials are prepared by removing the light-absorbing chromophores from natural wood, followed by infiltration of a refractive-index-matched polymer. The well-preserved hierarchical cellular structure of the wood substrate and the oriented nanocellulose reinforcement in the cell walls provide attractive load-bearing properties. The matching of the refractive index (RI) between polymer and bleached wood substrate improves optical transmittance. Those advantages, combined with the renewable resource origin, make TW a promising replacement for fossil-based plastics and some glasses in electronic equipment, optical devices and energy-saving buildings [2].

TW biocomposites were originally developed in 1992 to facilitate the visualization of the wood morphology [3]. Interest in TW was revitalized in 2016 in response to growing environmental concerns [4,5]. Since then, significant advances have been made in optimizing the fabrication procedures to produce material with controlled characteristics [6–10] (more sustainable [6,7], patternable [8], thick [9], or large[10]) and new functionalities [11–14] (photochromic [11], electrochromic [14], heat-shielding [13], magnetic [12], etc.). The optical transmittance of TW was enhanced by reducing absorption and defects via chemical treatment or using bio-based limonene acrylate with well-matched refractive index [7].

Experimental characterization of mechanics [15,16], optics [17], and heat transfer [10] of TW, is at the core of development of TW materials. The photon budget for TW composites was analyzed, combining theoretical modeling with experimental data [17]. The mismatch of the refractive indices (RI) for wood and the polymer phase was the main factor influencing optical properties [17]. Numerical simulation can contribute to understanding the parameter effects on the optical properties of TW. Several works have numerically studied the optical properties of fiber-based materials [18,19]. Kienle and Wetzel [18] used Monte Carlo simulations to investigate the optical properties in biological tissues containing aligned cylindrical and spherical scatterers. Similar model has been used to study the

optical scattering in native wood [20], but with significantly simplified 3D microstructural models. Schäfer and Kienle [19] studied the light scattering by multiple infinitely long parallel cylinders at perpendicular incidence using radiative transfer theory and analytical solutions of the Maxwell equations.

Accurate optical properties of TW are still challenging to simulate, partly because of the complex and variable cellular microstructure. The wood microstructure contains fibers, ray cells, and/or vessels with variations in size, orientation and other geometrical parameters. Optical properties of TW have previously been studied numerically using the Finite Element Method (FEM) [21]. A 2D model [21] was built from a 2D cross-sectional scanning electron microscope (SEM) image for ray scattering simulations. The 2D model was retrieved from micrographs of real microstructures. With this approach, parametric studies (such as the influence of cell wall thickness, and porosity) are difficult and sensitive to sample preparation and image noise. Also, the TW microstructure with tubular cells is highly anisotropic, so that scattering properties must be analyzed in 3D.

A recently proposed method [22] for high-fidelity 3D wood microstructure generation offers the possibility for 3D scattering simulations. The simulated 3D wood microstructures can describe major micro-scale features. Initial fibers and vessels are simply regular tubes. Well-designed distortion maps can then deform the ideal microstructures to mimic the interaction of different cells during wood formation (biosynthesis). Microstructural parameters can be independently controlled, such as cell wall thickness, fiber size, vessels and ray cell positions, lamination of wood veneers (thin layers), as well as refractive index mismatch between polymer and cell wall, etc.

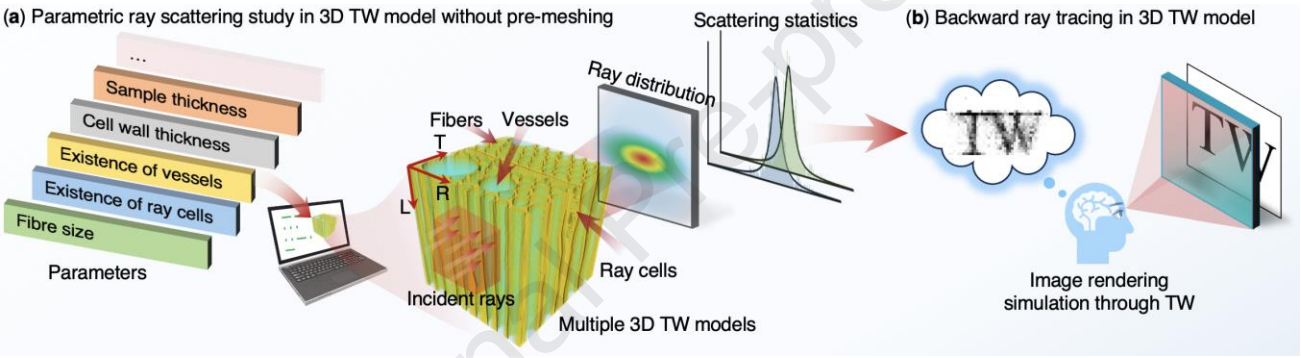

Figure 1. (a) Schematic description of 3D cellular structure modeling, ray scattering simulations and statistics of scattering patterns; (b) image rendering simulations based on backward ray tracing.

The present work numerically investigates the ray scattering resulting from wood-polymer refractive index mismatch using 3D TW models (Figure 1). Numerical studies of ray scattering in complex 3D TW microstructures using FEM is impractical due to the heavy computational burden of model meshing. Based on a geometrical optics [23] approach, we use classical ray tracing which does not require sample meshing to trace the ray path.

First, adaptable 3D wood microstructure models are generated based on real wood micrographs and different structural parameters [22] (Figure 1(a)). Assuming the TW samples have a native wood structure (without externally introduced defects inside, such as air voids), we anticipate the ray scattering results only from the RI mismatch between the wood substrate and polymer lumen (empty region at center of tubular cells). We numerically generate 1000 incident rays in the perpendicular direction (tangential T-direction, Figure 1(a)) to the LR plane. Then, we trace the complex ray paths in the 3D wood-polymer TW structure using ray tracing technique. In ray tracing, the key is to dynamically detect the material interface location and orientation for every small ray path interval using the support vector machine (SVM, see Section 2.3) [24] instead of meshing the complex 3D wood structure. The traced ray paths in the 3D TW microstructure describe the deviation of scattered rays through TW.

The objective is to develop a 3D modeling method and carry out simulations so that we can better understand how wood cell structure details influence light scattering in TW. This is important for selection of wood species (cell structures) and for materials design efforts (lamination, polymer selection, cell structure modification, etc.). The present ray tracing method can trace the ray path in very complex 3D microstructures. The effect of several parameters on the ray scattering in TW is investigated, including sample thickness, RI difference between two optical media, cell wall thickness, fiber diameter, and vessel or ray cell existence in TW composite as well as TW lamination (plywood

structure) (Figure 1(a)). Additionally, "virtual camera" rendering [25] through 3D TW is simulated to show the potential of ray scattering modeling (Figure 1(b)). This virtual camera simulation can predict the impression of an object when viewed through a TW window.

2. Methods

2.1 Generation of the realistic 3D model using a distortion-map-based method

A distortion-map-based method is used to generate a parametric wood microstructural model [22]. The 3D model is simulated by generating an initial backbone structure with uniform tubular cells and other features, followed by carefully designed local and global distortion mapping (see procedures in Supporting information S1. Wood microstructure generation). These specifically designed distortion maps can generate realistic features in the model, such as the insertion of the ray cells, the squeezing of the cells near the ray cells, the locally distorted fibers and vessels, the distortion of several large groups of fibers, twisting and/or bending of the whole structure. This model simulates the distribution of fibers, vessels and ray cells via controllable physical parameters. Different 3D wood microstructures can be generated by varying model parameters such as sample thickness, RI difference between polymer lumen and cell wall, fiber size, cell wall thickness, existence of vessels or ray cells and laminated TW veneer structures, etc.

2.2 Parametric study of scattering in 3D model

The ray propagation can be characterized by two parameters: the ray starting point in 3D space and the directional vector of the ray (e.g., corresponding to the Pointing vector). In our model, we consider 1000 incident rays perpendicularly bouncing the TW structures through a small region (size of 300×300 voxels, or ~150×150 μm see Figure 1(a)) on the LR plane. All rays will propagate inside 3D TW structures. We can trace the ray paths inside 3D TW and get the location and orientation distribution of the emergent rays (Section 2.3). Note that due to the complexity of light propagation, some rays cannot leave the TW structure from the LR plane at the exit side. Those rays will be ignored in our model. The impact of several parameters, including 1) TW thickness, 2) RI difference between wood substrate and polymer, 3) fiber size, 4) cell wall thickness, 5) the existence of vessel or ray cells, 6) TW laminate, on the ray scattering through 3D TW models are studied through simulation.

2.3 Ray tracing inside the 3D TW model

Considering the cell wall thickness, which is in the order of 1 μm, the geometric optics is still applicable to simulate the ray scattering in TW [21]. Based on geometrical optics, the ray will travel along the original orientation in the same optical medium. It will be deflected at the polymer lumen and cell wall interface due to the mismatch of the RI between the two compositions in TW, as shown in Figure 2(a) (only 2D model is presented for better visualization).

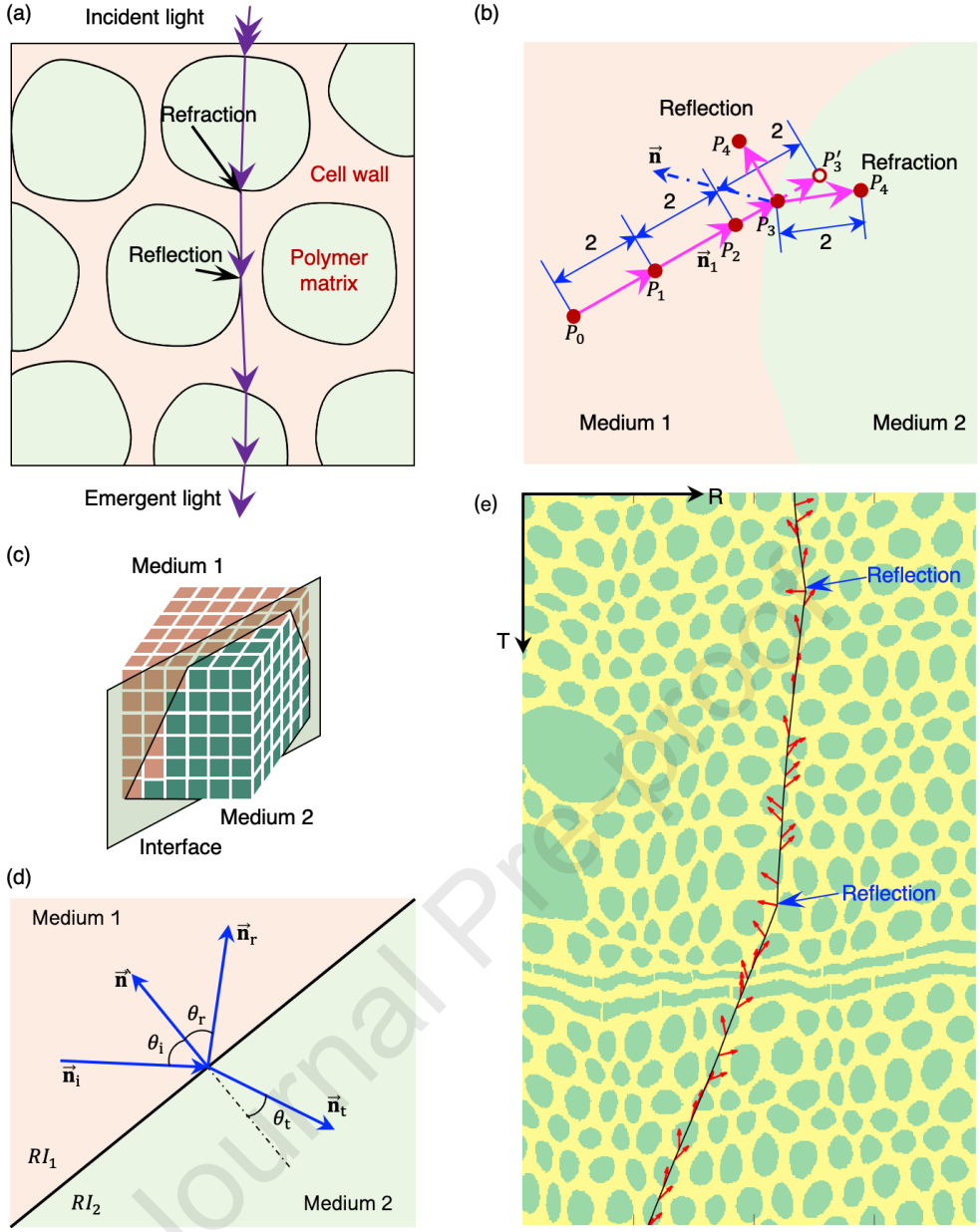

Figure 2. Ray tracing in TW: (a) Illustration of reflection or refraction on the interface; (b) the ray tracing method to trace the rays; (c) schematic of support vector machine for detecting the interface between two optical media; (d) principal diagram of Fresnel's law; (e) Illustration of ray propagation inside TW, where the rays are propagated inside 3D TW model, but only 2D projection is presented for better visualization. The detected interfaces on the ray path are labeled with red arrows, where the arrow orientations denote the normal vector of the interfaces.

To track the ray path, we track and update the ray position sequentially for every small path interval. Figure 2(b) shows that suppose a ray initiates from position P_0 along direction $\mathbf{n}_1$ (a 3D directional vector). We trace the ray forward along vector $\mathbf{n}_1$ for 2 voxels every distance step. The selection of the step size depends highly on the cell wall thickness. It should be smaller than the cell wall thickness. Then, it reaches position P_1. If P_0 and P_1 locate in the same medium, no interface exists between P_0 and P_1. The ray position should be updated to P_1 following the original direction $\mathbf{n}_1$.

We repeat this propagating step until the two consecutive points are located in two different optical media. It indicates an interface between these two points. We need to calculate the deflection (reflection or refraction) of the ray at the interface. As shown in Figure 2(b), P_2 and P_3' locate in two different media, and we suppose the middle point of line P_2P_3' as the intersection of the ray and the interface. If the normal vector of the interface is $\mathbf{n}$, the direction of the reflected or refracted ray could be calculated easily following Snell's equation. In this way, we can get the new position at point P_4. The ray path inside 3D TW model could be retrieved efficiently by updating the ray

positions consecutively.

The most significant step in ray tracing is to accurately determine the location and orientation of the interface between the two compositions in TW. Consider points P_2 and P_3' (Figure 2(b)) located in two optical media, a 6×6×6 voxels sub-volume (Figure 2(c)) nearing point P_3 is selected. The sub-volume size should be smaller than two times the cell wall thickness, since only one interface should exist in the sub-volume. It is reasonable to consider the interface as a plane inside this volume. Then, SVM [24], a classical and powerful classification algorithm in machine learning, is used to determine the separation interface [26] in this volume. In the small volume, the points belonging to two media are labeled as 1 and 0, respectively. The SVM algorithm can find a plane that best separates the two categories of points (Figure 2(c)).

The normal vector of the interface can be determined from the detected 3D plane equation. Though the intersection point on the surface can also be easily calculated from this detected plane, it may be incorrect in some cases. Especially when the interface is almost parallel with the incidental light, a small error on the estimated interface plane may lead to large error on the intersection point. For simplicity, we consider the intersection point as the middle point between P_2 and P_3'. The error, in this case, is smaller than 1 voxel.

Suppose the refraction index of medium 1 and medium 2 are RI_1 and RI_2, respectively, see Figure 2(d). Given the direction vector of the incident light to be $\vec{\mathbf{n}}_\mathrm{i}$. The ray will either be reflected or refracted at the interface.

According to Snell's equation, the refracted vector is calculated to

$$\vec{\mathbf{n}}_\mathrm{t} = \frac{RI_1}{RI_2}\vec{\mathbf{n}}_\mathrm{i} + \left(\frac{RI_1}{RI_2}\cos\theta_\mathrm{i} - \sqrt{1-\sin^2\theta_\mathrm{t}}\right)\vec{\mathbf{n}} \tag{1}$$

where

$$\sin^2\theta_\mathrm{t} = \left(\frac{RI_1}{RI_2}\right)^2(1-\cos^2\theta_\mathrm{i}) \tag{2}$$

Total reflection occurs at the interface when the incident angle is larger than the critical angle (or $\sin^2\theta_\mathrm{i} \geq \left(\frac{RI_2}{RI_1}\right)^2$). In that case, the incident angle θ_i should be identical to the reflection angle θ_r. We can easily get

$$\cos\theta_\mathrm{i} = -\vec{\mathbf{n}}\cdot\vec{\mathbf{n}}_\mathrm{i} \tag{3}$$

The direction vector of the reflected vector is calculated as

$$\vec{\mathbf{n}}_\mathrm{r} = \vec{\mathbf{n}}_\mathrm{i} - 2(\vec{\mathbf{n}}_\mathrm{i}\cdot\vec{\mathbf{n}})\cdot\vec{\mathbf{n}} \tag{4}$$

In Fresnel's law, the incident power will be separated at the interface. In TW, the refractive index difference is rather small between the two optical media. The reflected power at the cell wall-polymer interface is negligible when the incidental angle is smaller than the critical angle. Consequently, we neglect the reflection when the incidental angle is smaller than the critical angle, which introduces a very subtle deviation from Fresnel's law.

2.4 Rule of mixture for cell wall RI in TW

In literature, the RIs of cellulose fibrils are generally designated as the RIs of cell walls. Chen et al. [27] revealed the distribution of nanoscale polymer in the cell wall of TW, leading to a cell wall nanocomposite. Based on small-angle neutron scattering measurements, the fibrils with a diameter of 3 nm are distributed in a polymer matrix with a distance of around 7 nm. The volume ratio of fibril (considering only the RT plane) in the cell wall is calculated as 16.7% (Figure. S2). The RIs of polymer and cellulose are around 1.49 [1] and 1.54 [7], respectively, at a wavelength of 589 nm. The RI of the nanocomposite cell wall RI_w can be estimated using the rule of mixture [28] as

$$RI_\mathrm{w} = V_\mathrm{p}RI_\mathrm{p} + V_\mathrm{c}RI_\mathrm{c} = RI_\mathrm{p} + V_\mathrm{c}RI_\mathrm{d} \tag{5}$$

where V_p, V_c is the volume ratio of polymer and cellulose fibrils in cell wall, respectively; RI_p and RI_c are the RI of polymer lumen and cellulose, respectively; RI_d is the refractive index difference. RI_w is then calculated to be 1.4983. For simplicity, we use refractive difference as 0.01 in this work.

2.5 Statistical parameters to evaluate ray scattering

Figure. S1(a) shows the orientation distribution of the emergent rays scattered by TW samples (0.5 mm and 1.5 mm thick, respectively). The scattered rays distribute more homogeneously, especially along the R direction, for

thicker samples. The ray trajectories, combined with the angle distribution, offer a qualitative impression of the ray scattering of TW samples. Analyzing these results, statistic parameters can be retrieved to evaluate the scattering quantitively. Considering a sample with a thickness of 1 mm and an RI difference of 0.01, Figure. S1(b) shows the angle distribution (the yellow bars) of the scattered rays along R direction. We can estimate FWHM by fitting the distribution, if we assume the scattering of the emergent angle Θ_{emergent} approximately follows the Lorentz distribution (or Cauchy–Lorentz distribution) [29]:

$$f\left(\Theta_{\text{emergent}}; \Theta_0, \gamma\right) = \frac{1}{\pi}\left[\frac{\gamma}{\left(\Theta_{\text{emergent}} - \Theta_0\right)^2 + \gamma^2}\right] \tag{6}$$

where Θ_0 is the angle corresponding to the peak of the distribution; 2γ is the so-called FWHM, which is measured as the width of the angle distribution between those points which are half the maximum distribution amplitude. FWHM is used herein as an indicator to evaluate scattering. More significant scattering generally yields a larger FWHM.

Haze, a widely used scattering characterization parameter, measured as the ratio of scattered transmitted light (with emergent rays deviating more than 2.5°) to the total transmitted light, is also measured. The haze values in the simulation are then compared to the experimental results in the literature [9,10].

2.6 Virtual image rendering through TW

Tracing the ray paths leads to the possibility of simulating the imaging rendering through a piece of TW, or simulating how the object behind TW appears in our eyes. To this aim, a virtual camera or "virtual eye" is simulated (Figure 5(a)). Three different camera configurations are simulated. The first configuration generates image 1 in Figure 5(c). The camera has a focal length of 6.25 mm, an objective distance of 162.5 mm and a lens aperture diameter of 1 mm. The image sensor is 51×51 pixels with a pixel pitch of 0.5 μm. The TW sample (with wood parameters close to birch) has a dimension of width×length×thick = 1.5×1×0.5 mm. The RI was set to 1.54 for the cell wall and 1.53 for polymer. The object was fixed behind TW with a gap of 2 μm. The lens focuses on the object plane. Image 2 in Figure 5(c) is generated by adjusting the gap between the TW and the object plane as 100 μm. Image 3 is generated by first changing the focal length to 12.5 mm, and the objective distance to 137.5 mm. The object size is 0.5×0.5 mm for image 1 and 2 generation and 0.167×0.167 mm for image 3 rendering.

The images are generated using backward ray tracing (Figure 5(b)), a powerful tool being widely used in computer vision [30]. Considering a given pixel, 200 points in the lens aperture are randomly generated. The connections between these points and the pixel on the sensor are the ray paths inside this virtual camera. Then we can backward trace the ray paths through the 3D TW, and finally reach given points on the object (Supporting information S2. Backwards ray tracing for virtual image rendering). The existence of the TW will scatter those rays. Instead of focusing on a single point, these rays hit the object at different locations. The intensity at these points on the object can be easily interpolated. The image intensity on the sensor at the given pixel can be calculated as the average of the intensity of all 200 points on the object.

3. Results and discussion

3.1 3D TW microstructures

In previous work, we simulated ray scattering using 2D structures from micrographs of real wood materials [21]. It was concluded that the assumption of ray scattering was sufficient to address the present problem. 2D-modeling can, however, not explain anisotropic scattering, i.e., the elliptical shape of the scattered light beam at scattering material exit. The effects of different microstructural parameters (cell thickness, fiber size, existence of vessels, ray cells, etc.) on the scattering are also difficult to analyze based only on micrographs of real materials, partly since "new" microstructures often show changes in several parameters.

Multiple 3D TW microstructures based on hardwood features are generated at first based on the parameters summarized in Table 1. The parameters can be retrieved from real hardwood microscopy images to generate realistic wood microstructures. However, in a parametric study, we need to systematically study effects of different parameters.

The volume image scale of the theoretical wood structures is roughly 0.5 μm/voxel. The microstructures can be used to study scattering effects as a function of sample thickness, RI mismatch, fiber size, cell wall thickness, existence of ray cells and vessels, and in TW laminates. As one parameter is varied, the other parameters are constant.

Table 1. TW microstructures with hardwood features for parametric study of optical properties.

Study	TW thickness (mm)	RI difference	Wall thickness (μm)	Fiber diameter (mm)	Ray cells	Vessels	Laminate
1	0.25, 0.5,0.75,1,1.25,1.5	0.01	2	14.5	Yes	Yes	No
2	1	-0.03, -0.02, -0.01, 0.01, 0.02,0.03	2	14.5	Yes	Yes	No
3	1	0.01	2	14.5, 29	Yes	No	No
4	1	0.01	2, 4	29	Yes	Yes	No
5-1	1	0.01	2	14.5	Yes, No	Yes	No
5-2	1	0.01	2	14.5	Yes	Yes, No	No
6	0.5	0.01	2	14.5	Yes	Yes	No, [0/-45/90/45/0]

Typical TW substrates from hardwood species have complex microstructures (Figure 3 (a)). The 3D TW microstructures are generally described by three typical material orientations: longitudinal direction (L) along the wood fiber direction (tree height direction), tangential direction (T) (to circular tree stem cross section) and radial direction (R) (from center of tree stem). The ray cells are oriented in the R-direction. Note that the empty pore space in the cellular wood substrate is filled with polymer in the TW composite simulations.

The cellular, generic hardwood structures generated by the distortion-map-based method (Section 2.1) are shown in Figure 3 (b-f). To clearly show microstructural features, we present only sub-volumes with size 1000×1000×1000 voxels. Figure 3 (b) shows the cellular TW substrate microstructure with a cell wall thickness of 4 voxels and a fiber diameter of around 29 voxels, where pore space will be filled with a polymer phase in TW. In Figure 3 (c) and (d) ray cells and vessels, respectively, are removed. Figure 3 (e) shows the simulated microstructures with a cell wall thickness of 8 voxels and a fiber diameter of around 58 voxels. Figure 3 (f) shows a laminate [0/-45/90/45/0]. The structure includes 5 plies, and each ply has a cell wall thickness of 4 voxels and a fiber diameter of 29 voxels.

Complex features in wood microstructures, such as vessels, ray cells and fibers (Figure 3 (a)) are well represented in the 3D models (Figure 3 (b-f)). This includes variations in cell shape, typical of biological structures due to wood formation (biosynthesis) conditions [31]. The typical fibers are not perfect cylinders. Instead, the size and shape are distorted randomly to mimic the complexity of a real structure. The similar-sized fibers are prone to be spatially aggregated (Figure 3 (b)). Based on microscopy images of birch, single vessel, double-vessel clusters, and triple-vessel clusters are present in cellular microstructures generated. The ray cells are randomly distributed in the structures with different number of ray cells along longitudinal direction. The mimicking of realistic cellular structural features is a cornerstone for effective and accurate ray scattering simulations.

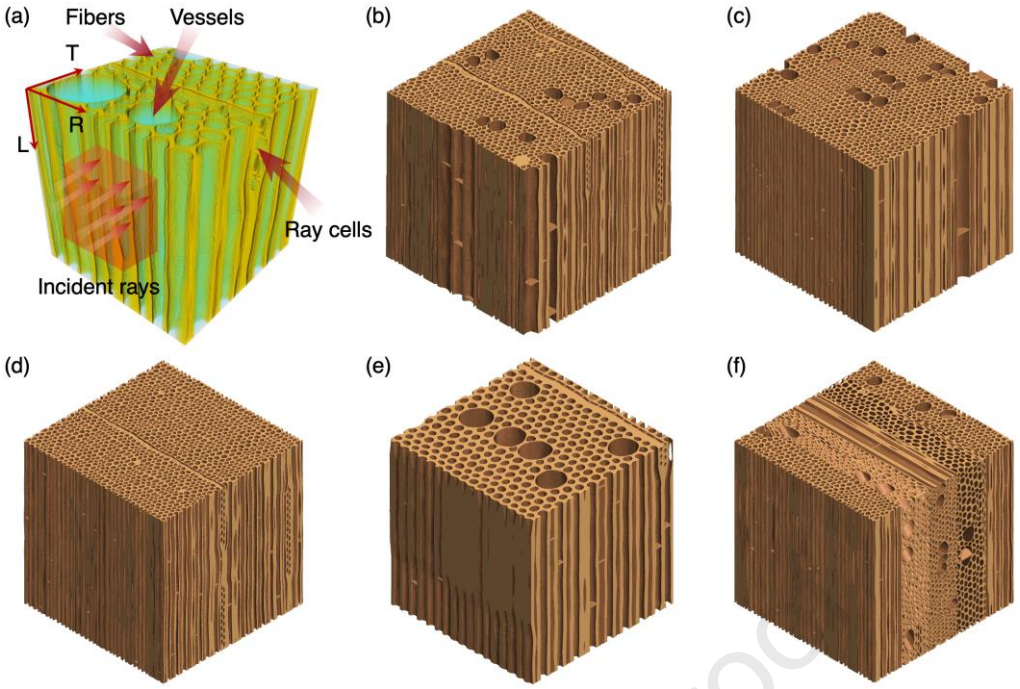

Figure 3. Examples of the generated 3D TW microstructures in this work. (a) Illustration of typical TW microstructure (L longitudinal, T tangential, R radial direction). (b-d) TW microstructure with cell wall thickness of 4 voxels and fiber diameter of around 29 voxels: the wood microstructure (b) with both vessels and ray cells, (c) with vessels but without ray cells, (e) with ray cells but without vessels. (e) TW microstructure with cell wall thickness of 8 voxels and fiber diameter of around 58 voxels. (f) TW laminate microstructure with cell wall thickness of 4 voxels and fiber diameter of around 29 voxels, where the laminate has 5 plies (layers).

3.2 Ray scattering in complex 3D TW models using ray tracing

In previous work, numerical simulation of the ray scattering required meshing of a 2D model [21]. Meshing large 3D TW two-phase microstructures, however, is computationally impractical. In this work, we numerically study the optical scattering from wood-polymer refractive index (RI) mismatch using ray tracing without meshing. Ray tracing is a powerful tool in 3D computer graphics that can model light transport. In ray tracing, the complex ray path of any ray inside a complex 3D structure can be numerically determined based on geometrical optics. We sequentially trace the ray paths in different 3D microstructures (Section 2.2) by updating their locations at every small optical path interval. The rays change their propagation orientation only at the interface between two optical phases. We detect and determine the material interfaces at every optical path interval using SVM, instead of implementing a pre-built fine mesh.

1000 incident rays are propagating through the 3D wood-polymer TW structure in the form of a beam (Figure 1(a)) in the perpendicular direction (tangential T-direction) to the LR plane. Typical fiber diameters are around 15 µm. For the largest microstructure, the thickness is 1.5 mm and the size of the RT square in Figure 3 (a) is 1.5×1 mm, except for the TW laminate (Figure 3 (f)) with a size of 0.5×0.5×0.5 mm. Figure 4(a) shows the ray paths for a given mismatch (RI difference of 0.01) in refractive index between wood and polymer phases (1.50-1.49, see Section 2.4). The projection of ray trajectories on the RT plane and LT plane (Figure 4(a)) reveals scattering anisotropy in TW. There is significant broadening of the beam in the radial R-direction (RT-plane), whereas there is almost no change in L-direction (LR-plane). The reason for broadening in R-direction is the “cylindrical” microscopic shape of fibers and vessels (see Figure 2 (e)). Once the ray paths are traced, the haze (ratio of scattered transmitted light to total transmitted light), see section 2.5) and the statistical parameter for full width at half maximum (FWHM, see Section 2.5) of the angular distribution of the transmitted rays along R and T directions are obtained (Figure 4(b-g)). Note that optical transmittance is not included in the discussion, since it is directly related to haze.

The FWHM of the ray scattering for the samples with different thicknesses is shown in Figure 4(b). The scattering in R-direction increases almost linearly with sample thickness. In L-direction, the scattering is much lower

but also increases nearly linearly with sample thickness. The pronounced anisotropic scattering arises from the orthotropic tubular microstructure of TW. In the RT plane, the normal vector of the "circular" interface is significantly different, see the red arrows in Figure 2 (e). The ray can meet the interface at very small angle so that the change in direction becomes large. The ray orientation change most significantly when the total reflection (see reflection in Figure 2 (e)) occurs.

In the LT plane, the lumen and the fiber cell wall interface are always almost along the L direction, which is perpendicular to the incident rays, so scattering is small. For a beam in the tangential direction, the rays are scattered more strongly in the R direction than in the L direction, because of the circular cross-section of wood fibers in the RT-plane.

The fiber size also plays an important role in ray scattering. Figure 4(c) shows ray scattering in microstructures with different fiber diameters. A doubling of fiber diameter significantly mitigates scattering in both directions. This is because the rays meet fewer interfaces. However, reduced fiber diameter does not necessarily result in increased scattering. When the fiber diameter is small enough, the lumen size could be negligible compared with cell wall thickness. The effect of fiber diameter on ray scattering needs further analysis, and should be related to experimental observations.

The influence of wood-polymer RI mismatch on scattering is presented in Figure 4(d). A larger RI difference leads to increased scattering (increased FWHM and haze). The FWHMs in both directions increase almost linearly with RI differences. The linear relationships no longer hold when FWHMs are relatively large. Figure 4(e) reveals that thicker cell walls may reduce scattering in both R and L directions. The reason is that thicker cell walls result in smaller inner lumen surface areas. It can reduce the probability of rays meeting the interface between wood and polymer phase.

Figure 4(f) presents the influence of vessels and ray cells on scattering (FWHM and haze). The scattering is more significant when the vessels are removed, because there will be a larger number of interfaces to redirect the rays. Removing ray cells will slightly reduce scattering in the L direction (from 0.99° to 0.96°), demonstrating that ray cells can increase L-direction scattering. The elliptical cross-sections of the ray cells are in the LT plane, which can redirect rays in the L direction like fibers can do in the RT plane. Additionally, the insertion of rays in the TW microstructure model will somewhat deform neighboring fibers oriented in the L-direction. Consequently, removing ray cells results in a slight reduction in scattering of optical rays in the L-direction.

Lamination is a classical way to produce plywood composites with less anisotropic hydromechanical properties. Figure 4(g) compares the scattering in a regular TW cellular structure and in a TW "plywood" laminate ($[0/-45/90/45/0]_T$) with the same thickness. The FWHM in Figure 4(g) shows that TW lamination can effectively provide more homogeneous and less anisotropic scattering. The scattering is very similar along L and R directions in the laminate. This homogenization effect has also been observed in a real TW laminate [32]. The scattering is still somewhat lower in the L direction than in the R-direction. The explanation is that the laminate has two plies of TW in 0°-direction but only one ply in 90°-direction.

Figure 4(c, e) is interesting. Doubling of fiber diameter and reduced cell wall thickness will both increase the lumen volume fraction (polymer content). However, increased fiber diameter reduces scattering by almost 50%, while reduced cell wall thickness (50%) increases scattering. This discrepancy suggests that volume fractions of wood and polymer are not necessarily governing parameters for ray scattering in TW.

One may note that a similar trend is observed for haze as for FWHM, see Figure 4(b-g). The haze for 0.75 mm thick birch sample in Figure 4(b) is numerically simulated to be 71.6% in this work, which is very close to the experimental data in Ref [9] (70% for 0.7 mm sample, RI difference, see Section 2.4). Balsa-based TW (cell wall thickness of around 1.2 μm, fiber radius of around 35.2 μm) shows lower haze (60.3%) in our simulation, which is similar to experimental data in Ref [10] (58% for 1 mm sample).

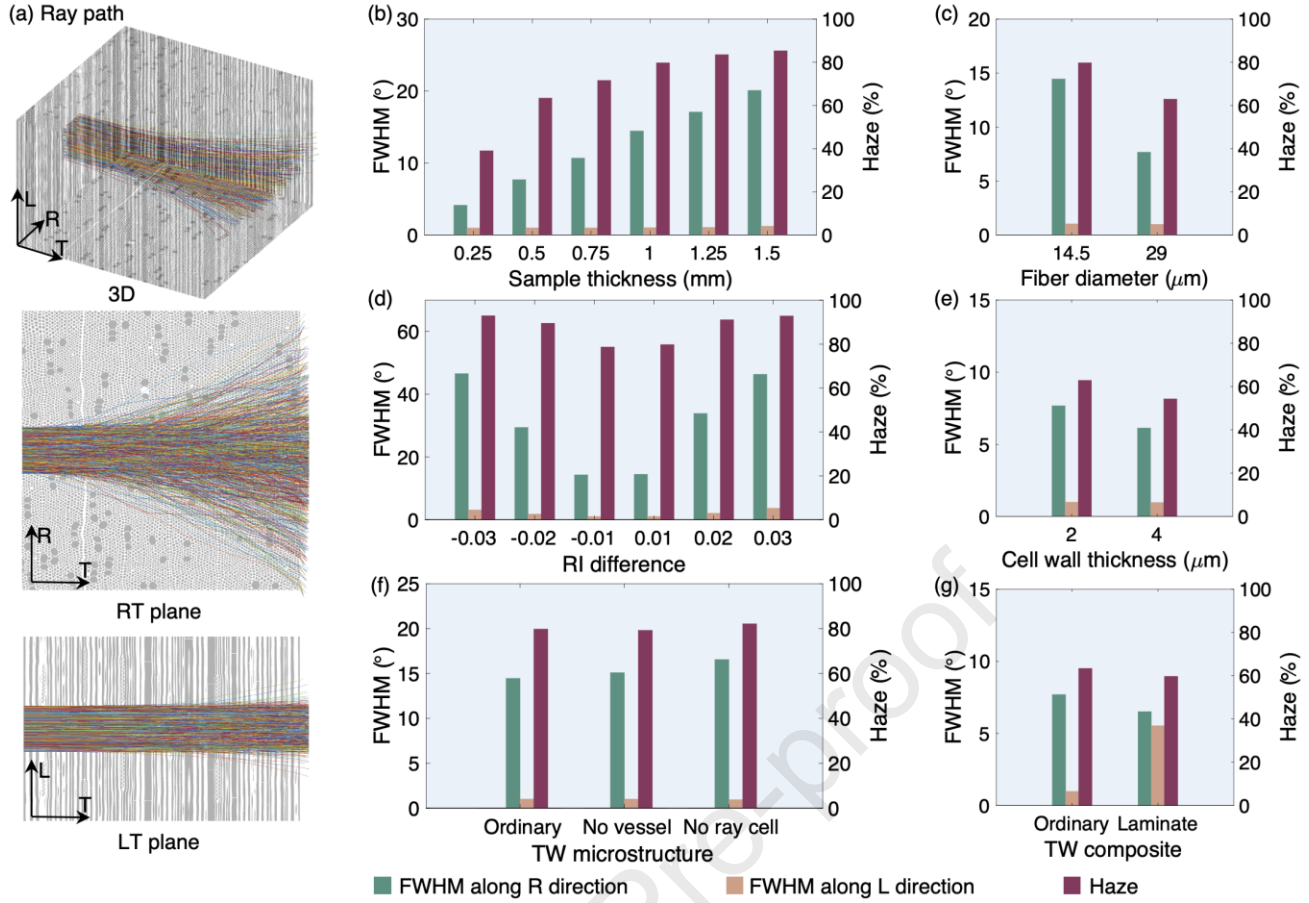

Figure 4. Ray tracing inside 3D TW model. a) the 3D ray trajectories of 1000 rays in a 1.5 mm TW sample and their projection on the RT and LT planes. Some rays are neglected if they cannot leave the sample from the other LR plane. The statistic scattering value, FWHM, of ray scattering and haze value (measure of extent of scattering) versus various geometrical, microstructural and material parameters: b) sample thickness, c) fiber diameter, d) RI difference, e) cell wall thickness, f) microstructures with or without vessels or ray cells, g) ordinary TW or laminate TW structure. Wood-polymer RI mismatch is fixed, except for (d), see Section 2.4. FWHM staple is green for R-direction, brown for L-direction and haze staple is burgundy.

The numerically calculated haze may not perfectly match that of real materials, which might be attributed to the defects (e.g., air gaps) in the materials, the simplification of the 3D microstructure model, and the simple geometric optics. The simulation, however, is effective to study the effect of RI mismatch between polymer and wood substrate. We now understand the origin of the elliptical beam exiting the specimen, and we can interpret differences between wood species.

3.3 Virtual camera simulation through transparent wood

The ray tracing method (see Section 2.3) is used to build an image of an object (see method description in Section 2.6) observed through a TW sheet (Figure 5(a)). A 0.5×0.5 mm object is placed at the focal plane behind the TW sheet. Virtual images are rendered through backward ray tracing (Figure 5(b)). The rendered images created by such a virtual camera or virtual eye are presented in Figure 5(c). Images of two objects with three different optical configurations are generated.

As expected, the characters are quite blurred from the ray scattering, but they are still recognizable. One needs to note that the characters are quite small, a scale where the influence of ray scattering is quite significant. Additionally, the blur of the horizontal and vertical lines on character “T” is notably different - the horizontal edges are much sharper than the vertical ones. This is due to the scattering anisotropy. The space between TW and the object is larger for image 2 than for image 1. Image 3 is rendered with a shorter objective distance and the same aperture diameter compared with that of image 1. The incident rays on TW that initiate from a single pixel have a larger incident angle

distribution for image 3, leading to larger scattering after passing through TW.

The simulation results validate the feasibility of this image rendering approach. Furthermore, the presented approach is generic and can be used for image formation by optical rays propagating through other complex scattering media. Given enough computational resources, this can be used to generate a large dataset for inverse haze prediction from simulated blurry images using deep learning.

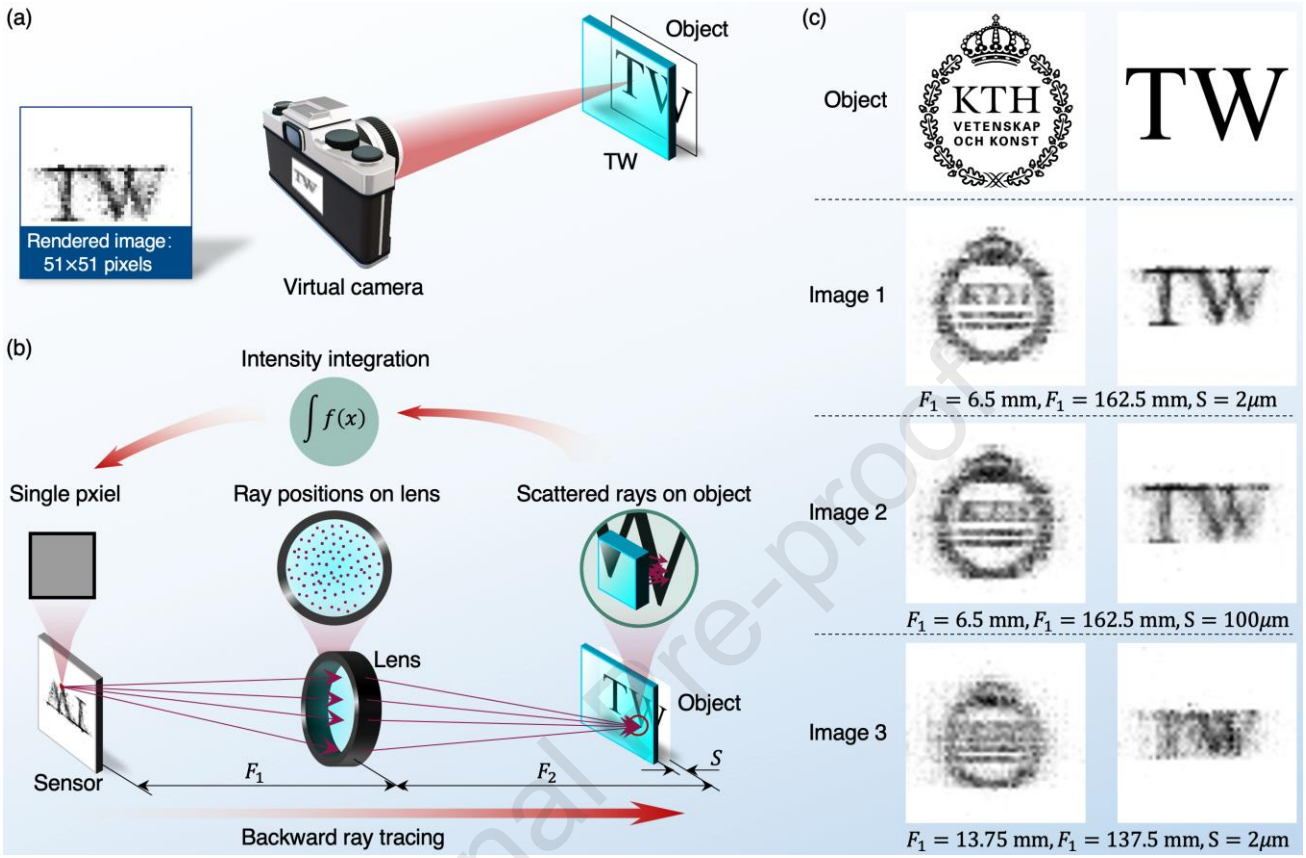

Figure 5. Virtual image rendering through transparent wood (TW). (a) Schematic diagram of a virtual camera for image rendering; (b) principal diagram to illustrate the principle of backward ray tracing for image rendering; (c) objects behind the TW sample are shown on the top, while the images generated with three different optical configurations are shown below.

4. Conclusions

"Transparent" biocomposites can be prepared from chemically pretreated wood substrates filled with a polymer. Light scattering in such composites is dominated by scattering events due to mismatch between wood and polymer refractive indices (RI). In some applications, it is of interest to control this scattering. Ray scattering in three-dimensional two-phase models of transparent birch composites (3D TW) was successfully investigated by ray tracing and mesh-free numerical simulations. The wood reinforcement phase was highly complex, as in the real birch microstructure, with connected cellular constituents such as fibers, vessels and ray cells as well as statistical variations in geometrical parameters. Due to high computational efficiency, a large number of 3D data sets (microstructure-ray scattering behavior for different RI mismatch) could be rapidly produced, of interest for deep learning simulations of composite materials.

A backward ray tracing method was developed to simulate a "virtual camera" or "virtual eye" to render images observed through 3D TW "windows". This bridges the gap between theoretical optical simulations and practical/ visual outcomes. Effects on "window function" from changes in cellular wood microstructures and/or RI differences can be simulated.

Systematic simulations of effects from variations in cellular microstructure parameters on scattering were performed, including wood-polymer RI differences. This is helpful for selection of wood substrates and for materials design. The parametric study led to the following structure-property results:

- Optical scattering in the RT plane is much larger than in the LT plane, since the 2D projection of the fiber in RT plane is circular. Some initially parallel rays will meet circular interfaces at random angles, which increases scattering. This explains the elliptical light pattern at exit, reported in many studies [33].
- Thicker TW samples show larger scattering, since the number of scattering interfaces increases with thickness
- Vessels reduce scattering whereas ray cells increase scattering.
- TW lamination effects can be predicted and can be used to control the distribution of the scattered light.
- The volume fraction of wood substrate is not a governing parameter for scattering in this model.

Supporting Information

Wood microstructure generation (Section S1); Backward ray tracing for virtual image rendering (Section S2); Ray scattering distribution (Figure S1); Rule of mixture for refractive index (Figure S2).
Rays propagating inside TW (MP4).

Data Availability

The data that support the findings of this study are available from the corresponding author upon reasonable request. The code for wood microstructure generation is available on GitHub (https://github.com/BinChenOPEN/Wood-Microstructure-Modeling).

Acknowledgements

The authors gratefully acknowledge the support from Knut and Alice Wallenberg foundation (KAW 2021.0311) and HORIZON AI-TRANSPWOOD (AI-Driven Multiscale Methodology to Develop Transparent Wood as Sustainable Functional Material) project, Grant no. 101138191, co-funded by the European Union. The authors would like to thank Dr. Céline Montanari for the SEM images of the birch.

Conflict of Interests

The authors declare no competing interests.

Reference

[1] Y. Li, E. Vasileva, I. Sychugov, S. Popov, L. Berglund, Optically Transparent Wood: Recent Progress, Opportunities, and Challenges, Adv Opt Mater 6 (2018). https://doi.org/10.1002/adom.201800059.

[2] C. Chen, Y. Kuang, S. Zhu, I. Burgert, T. Keplinger, A. Gong, T. Li, L. Berglund, S.J. Eichhorn, L. Hu, Structure–property–function relationships of natural and engineered wood, Nat Rev Mater 5 (2020) 642–666. https://doi.org/10.1038/s41578-020-0195-z.

[3] S. Fink, Transparent Wood – A New Approach in the Functional Study of Wood Structure, Holzforschung 46 (1992) 403–408. https://doi.org/10.1515/hfsg.1992.46.5.403.

[4] Y. Li, Q. Fu, S. Yu, M. Yan, L. Berglund, Optically Transparent Wood from a Nanoporous Cellulosic Template: Combining Functional and Structural Performance, Biomacromolecules 17 (2016) 1358–1364. https://doi.org/10.1021/acs.biomac.6b00145.

[5] M. Zhu, J. Song, T. Li, A. Gong, Y. Wang, J. Dai, Y. Yao, W. Luo, D. Henderson, L. Hu, Highly Anisotropic, Highly Transparent Wood Composites, Advanced Materials 28 (2016) 5181–5187. https://doi.org/10.1002/adma.201600427.

[6] Y. Li, Q. Fu, R. Rojas, M. Yan, M. Lawoko, L. Berglund, Lignin-Retaining Transparent Wood, ChemSusChem 10 (2017) 3445–3451. https://doi.org/10.1002/cssc.201701089.

[7] C. Montanari, Y. Ogawa, P. Olsén, L.A. Berglund, High Performance, Fully Bio-Based, and Optically

Transparent Wood Biocomposites, Advanced Science 8 (2021) 2100559. https://doi.org/10.1002/advs.202100559.

[8] Q. Xia, C. Chen, T. Li, S. He, J. Gao, X. Wang, L. Hu, Solar-assisted fabrication of large-scale, patternable transparent wood, Sci Adv 7 (2021) 1–9. https://doi.org/10.1126/sciadv.abd7342.

[9] Y. Li, X. Yang, Q. Fu, R. Rojas, M. Yan, L. Berglund, Towards centimeter thick transparent wood through interface manipulation, J Mater Chem A Mater 6 (2018) 1094–1101. https://doi.org/10.1039/c7ta09973h.

[10] X. Wang, T. Zhan, Y. Liu, J. Shi, B. Pan, Y. Zhang, L. Cai, S.Q. Shi, Large-Size Transparent Wood for Energy-Saving Building Applications, ChemSusChem 11 (2018) 4086–4093. https://doi.org/10.1002/cssc.201801826.

[11] L. Wang, Y. Liu, X. Zhan, D. Luo, X. Sun, Photochromic transparent wood for photo-switchable smart window applications, J Mater Chem C Mater 7 (2019) 8649–8654. https://doi.org/10.1039/c9tc02076d.

[12] W. Gan, L. Gao, S. Xiao, W. Zhang, X. Zhan, J. Li, Transparent magnetic wood composites based on immobilizing Fe3O4 nanoparticles into a delignified wood template, J Mater Sci 52 (2017) 3321–3329. https://doi.org/10.1007/s10853-016-0619-8.

[13] Z. Yu, Y. Yao, J. Yao, L. Zhang, Z. Chen, Y. Gao, H. Luo, Transparent wood containing CsXWO3 nanoparticles for heat-shielding window applications, J Mater Chem A Mater 5 (2017) 6019–6024. https://doi.org/10.1039/c7ta00261k.

[14] A.W. Lang, Y. Li, M. De Keersmaecker, D.E. Shen, A.M. Österholm, L. Berglund, J.R. Reynolds, Transparent Wood Smart Windows: Polymer Electrochromic Devices Based on Poly(3,4-Ethylenedioxythiophene):Poly(Styrene Sulfonate) Electrodes, ChemSusChem 11 (2018) 854–863. https://doi.org/10.1002/cssc.201702026.

[15] E. Jungstedt, C. Montanari, S. Östlund, L. Berglund, Mechanical properties of transparent high strength biocomposites from delignified wood veneer, Compos Part A Appl Sci Manuf 133 (2020) 105853. https://doi.org/10.1016/j.compositesa.2020.105853.

[16] E. Jungstedt, S. Östlund, L.A. Berglund, Transverse fracture toughness of transparent wood biocomposites by FEM updating with cohesive zone fracture modeling, Compos Sci Technol 225 (2022) 1–10. https://doi.org/10.1016/j.compscitech.2022.109492.

[17] H. Chen, C. Montanari, R. Shanker, S. Marcinkevicius, L.A. Berglund, I. Sychugov, Photon Walk in Transparent Wood: Scattering and Absorption in Hierarchically Structured Materials, Adv Opt Mater 10 (2022). https://doi.org/10.1002/adom.202102732.

[18] A. Kienle, C. Wetzel, A. Bassi, D. Comelli, P. Taroni, A. Pifferi, Determination of the optical properties of anisotropic biological media using isotropic and anisotropic diffusion models, Optics InfoBase Conference Papers 12 (2007) 1–9. https://doi.org/10.1117/12.728323.

[19] J. Schäfer, A. Kienle, Scattering of light by multiple dielectric cylinders: comparison of radiative transfer and Maxwell theory, Opt Lett 33 (2008) 2413. https://doi.org/10.1364/ol.33.002413.

[20] A. Kienle, C. D'Andrea, F. Foschum, P. Taroni, A. Pifferi, Light propagation in dry and wet softwood, Opt Express 16 (2008) 9895. https://doi.org/10.1364/oe.16.009895.

[21] J. Pang, A. Baitenov, C. Montanari, A. Samanta, L. Berglund, S. Popov, I. Zozoulenko, Light Propagation in Transparent Wood: Efficient Ray-Tracing Simulation and Retrieving an Effective Refractive Index of Wood Scaffold, Adv Photonics Res 2 (2021) 2100135. https://doi.org/10.1002/adpr.202100135.

[22] B. Chen, C. Montanari, S. Popov, L.A. Berglund, A distortion-map-based method for morphology generation in multi-phase materials - application to wood, Compos Sci Technol 244 (2023) 110262. https://doi.org/10.1016/j.compscitech.2023.110262.

[23] Ray Optics, in: Fundamentals of Photonics, John Wiley & Sons, Ltd, 1991: pp. 1–40. https://doi.org/https://doi.org/10.1002/0471213748.ch1.

[24] W.S. Noble, What is a support vector machine?, Nat Biotechnol 24 (2006) 1565–1567. https://doi.org/10.1038/nbt1206-1565.

[25] A. Lumsdaine, Focused plenoptic camera and rendering, J Electron Imaging 19 (2010) 021106.

https://doi.org/10.1117/1.3442712.

[26] B. Wohlberg, D.M. Tartakovsky, A. Guadagnini, Subsurface characterization with support vector machines, IEEE Transactions on Geoscience and Remote Sensing 44 (2006) 47–57. https://doi.org/10.1109/TGRS.2005.859953.

[27] P. Chen, Y. Li, Y. Nishiyama, S.V. Pingali, H.M. O'Neill, Q. Zhang, L.A. Berglund, Small Angle Neutron Scattering Shows Nanoscale PMMA Distribution in Transparent Wood Biocomposites, Nano Lett 21 (2021) 2883–2890. https://doi.org/10.1021/acs.nanolett.0c05038.

[28] H. Hemmati, R. Magnusson, Development of tuned refractive-index nanocomposites to fabricate nanoimprinted optical devices, Opt Mater Express 8 (2018) 175. https://doi.org/10.1364/ome.8.000175.

[29] J. Wu, Y. Peng, Y. Li, W. Wang, J. Chen, S. Dhakal, Prediction of beef quality attributes using VIS/NIR hyperspectral scattering imaging technique, J Food Eng 109 (2012) 267–273. https://doi.org/10.1016/j.jfoodeng.2011.10.004.

[30] N. Horiuchi, Integrated optical antenna, Nat Photonics 14 (2020) 134. https://doi.org/10.1038/s41566-020-0594-0.

[31] C. Plomion, G. Leprovost, A. Stokes, Wood Formation in Trees, Plant Physiol 127 (2001) 1513–1523. https://doi.org/10.1104/pp.010816.

[32] Q. Fu, M. Yan, E. Jungstedt, X. Yang, Y. Li, L.A. Berglund, Transparent plywood as a load-bearing and luminescent biocomposite, Compos Sci Technol 164 (2018) 296–303. https://doi.org/10.1016/j.compscitech.2018.06.001.

[33] Y. Li, Q. Fu, X. Yang, L. Berglund, Transparent wood for functional and structural applications, Philosophical Transactions of the Royal Society A: Mathematical, Physical and Engineering Sciences 376 (2018). https://doi.org/10.1098/rsta.2017.0182.

Highlights

Effects of different parameters on light scattering of transparent wood are studied.

Distortion-map-based method simulates various 3D transparent wood structures.

Ray tracing simulates the scattering in different 3D transparent wood structures.

Backward ray tracing mimics the blurring effect through a transparent wood.

Declaration of Interest Statement

The authors declared that they have no conflicts of interest to this work.